



# The concept of global monsoon applied to the last glacial maximum: A multi-model analysis



Dabang Jiang <sup>a, b, e, \*</sup>, Zhiping Tian <sup>a</sup>, Xianmei Lang <sup>a, b, c</sup>, Masa Kageyama <sup>d</sup>, Gilles Ramstein <sup>d</sup>

<sup>a</sup> Institute of Atmospheric Physics, Chinese Academy of Sciences, Beijing 100029, China

<sup>b</sup> CAS Center for Excellence in Tibetan Plateau Earth Sciences, Beijing 100101, China

<sup>c</sup> Collaborative Innovation Center on Forecast and Evaluation of Meteorological Disasters, Nanjing University of Information Science & Technology (NUIST), Nanjing 210044, China

<sup>d</sup> LSCE/IPSL, UMR CEA-CNRS-UVSQ 8212, CE Saclay, L'Orme des Merisiers, Bâtiment 701, 91191 Gif-sur-Yvette Cedex, France

<sup>e</sup> Joint Center for Global Change Studies, Beijing 100875, China

## ARTICLE INFO

### Article history:

Received 12 August 2014

Received in revised form

13 August 2015

Accepted 31 August 2015

Available online xxx

### Keywords:

Last glacial maximum

Global monsoon

PMIP

Simulation

## ABSTRACT

The last glacial maximum (LGM, ca. 21,000 years ago) has been extensively investigated for better understanding of past glacial climates. Global-scale monsoon changes, however, have not yet been determined. In this study, we examine global monsoon area (GMA) and precipitation (GMP) as well as GMP intensity (GMPI) at the LGM using the experiments of 17 climate models chosen from the Paleoclimate Modelling Intercomparison Project (PMIP) according to their ability to reproduce the present global monsoon climate. Compared to the reference period (referring to the present day, ca. 1985, for three atmospheric plus two atm–slab ocean models and the pre-industrial period, ca. 1750, for 12 fully coupled atmosphere–ocean or atmosphere–ocean–vegetation models), the LGM monsoon area increased over land and decreased over the oceans. The boreal land monsoon areas generally shifted southward, while the northern boundary of land monsoon areas retreated southward over southern Africa and South America. Both the LGM GMP and GMPI decreased in most of the models. The GMP decrease mainly resulted from the reduced monsoon precipitation over the oceans, while the GMPI decrease was derived from the weakened intensity of monsoon precipitation over land and the boreal ocean. Quantitatively, the LGM GMP deficit was due to, first, the GMA reduction and, second, the GMPI weakening. In response to the LGM large ice sheets and lower greenhouse gas concentrations in the atmosphere, the global surface and tropospheric temperatures cooled, the boreal summer meridional temperature gradient increased, and the summer land–sea thermal contrast at 40°S – 70°N decreased. These are the underlying dynamic mechanisms for the LGM monsoon changes. Qualitatively, simulations agree with reconstructions in all land monsoon areas except in the western part of northern Australia where disagreements occur and in South America and the southern part of southern Africa where there is uncertainty in reconstructions. Simulations do not support an inter-hemispheric anti-phasing of monsoon intensity change as suggested by proxy data.

© 2015 Elsevier Ltd. All rights reserved.

## 1. Introduction

The concept of “Global Monsoon” has developed over the last few decades to describe how the ensemble of regional monsoon systems, taken together, constitutes a core component of the global energy and water cycle (Webster et al., 1998; Trenberth et al., 2000;

\* Corresponding author. Institute of Atmospheric Physics, Chinese Academy of Sciences, Beijing 100029, China.

E-mail address: [jiangdb@mail.iap.ac.cn](mailto:jiangdb@mail.iap.ac.cn) (D. Jiang).

Wang and Ding, 2008; Wang, 2009). Monsoons can be viewed from a global perspective because they are a forced response to the annual cycle of the solar heating and are thus a global phenomenon in essence (Trenberth et al., 2000; Wang, 2009; Cheng et al., 2012; Wang et al., 2012). This concept has first been developed for describing the present-day mean annual cycle and then applied to study recent monsoon changes (e.g., Webster et al., 1998; Wang et al., 2012).

Due to their being a major feature of the tropical hydrological cycle and atmospheric circulation, individual monsoons have been

extensively studied from paleo-records and have been shown to vary widely (e.g., Schulz et al., 1998; Baker et al., 2001; Weldeab et al., 2007; Wang et al., 2008; An et al., 2011). Regional monsoon changes have been proposed to be linked on orbital timescales, for example, between the Asian and South American monsoons (Wang et al., 2004; Cheng et al., 2012) and between the northern and southern African monsoons (Partridge et al., 1997). Can the “Global Monsoon” concept then be applied to characterize and analyse monsoon changes on longer timescales than those for which the concept has been developed? Following our recent simulation analysis of the interglacial global monsoon during the mid-Holocene (Jiang et al., 2015), in the present study we examine if this concept holds for a glacial climate very different from today: the climate of the last glacial maximum (LGM, ca. 21,000 years ago). The LGM refers to the interval during the last glacial period when the global volume of ice sheets was at its greatest, and it provides a good opportunity for an insight into the glacial climate system.

Based on geological records at individual sites, orbital-scale monsoon evolution has been discussed at the local or regional scale. For the LGM, the boreal summer monsoon is generally inferred to have weakened in northern Africa (e.g., Weldeab et al., 2007; Tjallingii et al., 2008; Ziegler et al., 2010), the northern Arabian Sea (e.g., Schulz et al., 1998), India (e.g., An et al., 2011; Saraswat et al., 2014), and East Asia (e.g., Liu and Ding, 1998; Jian et al., 2001; Wang et al., 2008), while the opposite generally holds true for the austral summer monsoon in tropical South America (e.g., Baker et al., 2001; Wang et al., 2004; Cheng et al., 2012). As will be reviewed later in this work, the LGM monsoon and/or climatological annual precipitation are generally estimated, from the available proxy data, to weaken or decrease in all land monsoon areas worldwide, except in South America and the southern part of southern Africa where there is uncertainty in reconstructions (please refer to Section 4.6). These changes at individual sites have typically been attributed to orbital forcing, atmospheric greenhouse gas concentrations, and high-latitude ice volume through the intercomparison of sparse proxy data and their match with orbital forcing on varying timescales, although the underlying dynamic processes remain less explored. The concept of global monsoon could help better explore the links between the different regional monsoon changes from LGM to the pre-industrial periods. This is the central topic of this study.

On the modelling side, the LGM has been one of the key periods within the Paleoclimate Modelling Intercomparison Project (PMIP). While the first PMIP phase (PMIP1) was based on the use of atmosphere-only or atm–slab ocean model experiments, phases 2 (PMIP2) and 3 (PMIP3) were based on coupled climate models. PMIP3 simulations have been integrated in the Coupled Model Intercomparison Project phase 5 (CMIP5) exercise (Taylor et al., 2012), and they have thus been performed with the same model versions as those used for climate projections. It has been found that climate models are able to reproduce generally colder and drier conditions and large-scale changes in atmospheric circulation for that period, indicating their adequate representation of the major processes, although the simulated magnitude of regional changes still differs in certain respects from reconstructions (e.g., Braconnot et al., 2012; Masson-Delmotte et al., 2013). More specifically for monsoon, an atmospheric model-simulated low-level winds and precipitation decrease in southern Asia, while precipitation increases in equatorial northern Africa (Prell and Kutzbach, 1987). Seven atmospheric models within PMIP1 reproduce weakened monsoon circulation and decreased precipitation in West Africa over 20°W–30°E (Braconnot et al., 2000). Reduced precipitation and weakened low-level meridional winds are characteristic responses over East Asia in both atmospheric and coupled models within PMIP1/2 (Yanase and Abe-Ouchi, 2007; Zhou and Zhao,

2009; Jiang and Lang, 2010).

Previous analyses of the simulations of the LGM monsoons have primarily focused on Africa and Asia. Monsoon precipitation has been calculated based on fixed land areas defined based on modern climatology. This could be inappropriate given the fact that glacial monsoon areas differ from those of the present day, although we do not currently know what the difference is like. Moreover, little or no attention has been paid to the land monsoon areas of North America, southern Africa, northern Australia, and South America, and no attention to ocean monsoon areas. In the present work, we aim at presenting a review of the state-of-the-art climate model performance in simulating regional monsoon changes, including for those areas which have been less studied than the African or Asian monsoon, and at presenting these monsoon changes in the comprehensive framework of the global monsoon. We also consider the results from the previous phases of the PMIP project to build a more complete review and examine whether, from one generation to the other, model results change significantly when compared in a single framework.

Based on the above, here we present an analysis of the LGM monsoon using experiments of multiple climate models, including those participating in the latest CMIP5. The questions to address are: (1) How do global monsoon diagnostics (land and ocean monsoon areas, monsoon precipitation, and monsoon precipitation intensity) respond to the LGM forcing at regional, hemispheric, and global scales? (2) What are the dynamic mechanisms involved in the most common changes among the simulations? (3) To what extent are simulations consistent with reconstructions over large-scale land monsoon areas?

## 2. Data and methods

### 2.1. Model and observation data

This study uses the available experiments of the LGM climate within PMIP, which are performed by eight atmospheric models and nine atm–slab ocean models within PMIP1, seven fully coupled atmosphere–ocean or atmosphere–ocean–vegetation models (hereafter referred to as coupled models) within PMIP2, and nine coupled models within PMIP3. The boundary conditions include changes in the Earth's orbital parameters, ice-sheet extent, topography, land–sea mask, and atmospheric concentrations of greenhouse gases with respect to the reference period, which refers to the present day, ca. 1985, for PMIP1 and the pre-industrial period, ca. 1750, for PMIP2/3. Basic information about the climate models and data is provided in Table 1. More details about the models and experiments are available online at <http://pmip3.lscce.ipsl.fr/>.

The long-term mean precipitation of the Version-2.2 Global Precipitation Climatology Project monthly precipitation analysis for the period 1979–2000 (Huffman et al., 2009; hereafter referred to as observation) is used to assess the ability of the models. To measure the monsoon areas and their changes at fine horizontal resolution, all simulated and observational data are interpolated to a horizontal grid resolution of 0.5° latitude by 0.5° longitude using bilinear interpolation.

### 2.2. Definition of global monsoon area, precipitation, and intensity

Following Liu et al. (2009) and Wang et al. (2012), the global monsoon area (GMA) is defined as the region where the local summer-minus-winter precipitation exceeds 2 mm day<sup>-1</sup> and the local summer rainfall exceeds 55% of annual total precipitation. The summer spans May through September (May–September) for the northern hemisphere and November through March (November–March) for the southern hemisphere. The global monsoon

**Table 1**  
Basic information about the climate models and experiments used in this study.

Model ID	Model type	Atmospheric resolution	Length of run analysed (year)	
<b>Eight atmospheric models plus nine atm–slab ocean models suffixed with –slab within PMIP1</b>				
01	CCC2.0	Atmosphere only	3.75° × ~3.7°, L10	10
02	CCC2.0-slab	Atmosphere–slab ocean	3.75° × ~3.7°, L10	10
03	CCM1-slab	Atmosphere–slab ocean	7.5° × ~4.4°, L12	10
04	CCSR1	Atmosphere only	~5.6° × 5.5°, L20	10
05	ECHAM3	Atmosphere only	~2.8° × 2.8°, L19	10
06	GEN1-slab	Atmosphere–slab ocean	7.5° × ~4.4°, L12	14
07	GEN2	Atmosphere only	3.75° × ~3.7°, L18	10
08	GEN2-slab	Atmosphere–slab ocean	3.75° × ~3.7°, L18	10
09	GFDL-slab	Atmosphere–slab ocean	3.75° × ~2.2°, L20	25
10	LMCELM4	Atmosphere only	7.5° × ~3–10°, L11	15
11	LMCELM4-slab	Atmosphere–slab ocean	7.5° × ~3–10°, L11	15
12	LMCELM5	Atmosphere only	~5.6° × 2.3–8.5°, L11	15
13	MRI2	Atmosphere only	5° × 4°, L15	10
14	MRI2-slab	Atmosphere–slab ocean	5° × 4°, L15	14
15	UGAMP	Atmosphere only	~2.8° × 2.8°, L19	20
16	UGAMP-slab	Atmosphere–slab ocean	~2.8° × 2.8°, L19	20
17	UKMO-slab	Atmosphere–slab ocean	3.75° × 2.5°, L19	20
<b>Seven coupled models within PMIP2</b>				
18	CCSM3.0	Atmosphere–full ocean	~2.8° × 2.8°, L18	50
19	CNRM-CM3.3	Atmosphere–full ocean	~2.8° × 2.8°, L31	100
20	FGOALS-1.0 g	Atmosphere–full ocean	~2.8° × 3–6°, L9	100
21	HadCM3M2	Atmosphere–full ocean	3.75° × 2.5°, L19	100
22	HadCM3M2-gvm	Atmosphere–ocean–vegetation	3.75° × 2.5°, L19	100
23	IPSL-CM4-V1-MR	Atmosphere–full ocean	3.75° × 2.5°, L19	100
24	MIROC3.2	Atmosphere–full ocean	~2.8° × 2.8°, L20	100
<b>Nine coupled models within PMIP3 (here we use only the first run of each model to treat all models equally)</b>				
25	CCSM4	Atmosphere–full ocean	1.25° × ~0.9°, L26	301
26	CNRM-CM5	Atmosphere–full ocean	~1.4° × 1.4°, L31	200
27	COSMOS-ASO	Atmosphere–ocean–vegetation	3.75° × ~3.7°, L19	600
28	FGOALS-g2	Atmosphere–ocean–vegetation	~2.8° × 3–6°, L26	100
29	GISS-E2-R	Atmosphere–full ocean	2.5° × 2°, L40	100
30	IPSL-CM5A-LR	Atmosphere–ocean–vegetation	3.75° × ~1.9°, L39	500
31	MIROC-ESM	Atmosphere–ocean–vegetation	~2.8° × 2.8°, L80	100
32	MPI-ESM-P	Atmosphere–full ocean	1.875° × ~1.9°, L47	100
33	MRI-CGCM3	Atmosphere–full ocean	1.125° × ~1.1°, L48	100

precipitation (GMP) is expressed as the sum of total summer rainfall in the GMA, namely the May–September rainfall in the boreal monsoon area plus the November–March rainfall in the austral monsoon area (Hsu et al., 2012). The global monsoon precipitation intensity (GMPI) is measured by area-averaged summer rainfall in the GMA (Hsu et al., 2012; Wang et al., 2012).

### 3. Evaluation of climate models for the present monsoon-related precipitation

Since the extent to which climate models reproduce the geographical distribution, magnitude, and spatial variability of the reference period annual, summer, and winter precipitation climatology at the low- and mid-latitudes determines the confidence of their results for the past monsoon climate, the reliability of climate models is first evaluated against observation. This evaluation is based on 158,400 grid points between 40°S and 70°N where these boundaries are chosen according to the modern GMA obtained from both simulations and observation. Fig. 1 illustrates the range of spatial correlation coefficients (0.18–0.87), normalised standard deviations (0.22–1.58), and normalised centred root-mean-square differences (0.56–1.15). Considering that several models fail to reasonably capture the spatial pattern and variability of the observed precipitation, two criteria are set to identify relatively reliable models. First, the normalised standard deviation must be greater than 0.5 and less than 1.5; and second, the normalised centred root-mean-square difference must be less than 1.0. Accordingly, six models (GEN1-slab, LMCELM4, LMCELM4-slab, LMCELM5, UGAMP, and UGAMP-slab) are excluded. Besides,

because the local summer, winter, and annual precipitation amounts are involved to distinguish the monsoon area, whether they can be reliably simulated by the remaining 27 models is further examined in the boreal, austral, and global monsoon areas identified by observation. Fig. 2 illustrates that the area-averaged precipitation varies with model. As such, the requirement of being within  $\pm 75\%$  deviations of the observed values is set to screen models. Ten models (CCC2.0-slab, CCM1-slab, GEN2, MRI2, MRI2-slab, UKMO-slab, CNRM-CM3.3, HadCM3M2, HadCM3M2-gvm, and COSMOS-ASO) are thus filtered out.

Based on the above steps, five of 17 PMIP1, four of seven PMIP2, and eight of nine PMIP3 models are retained for analysis (Fig. 2), indicating a general improvement of climate models for global monsoon climate from PMIP1 via PMIP2 to PMIP3. The arithmetic mean of 17 chosen models performs well in reproducing the observed spatial pattern and spatial variability of the summer, winter, and annual precipitation at the low- and mid-latitudes and in the GMA. As seen in Fig. 1, the 17-model arithmetic mean has a higher reliability than all individual models and is therefore emphasised in the subsequent analysis.

## 4. LGM changes in global monsoon

### 4.1. LGM global monsoon area

The LGM GMA was slightly changed against the reference period, as it decreased by 4.8% averaged for all 17 models and roughly half of the models reproduced an increase or decrease (Fig. 3a). Monsoon areas generally increased over land and

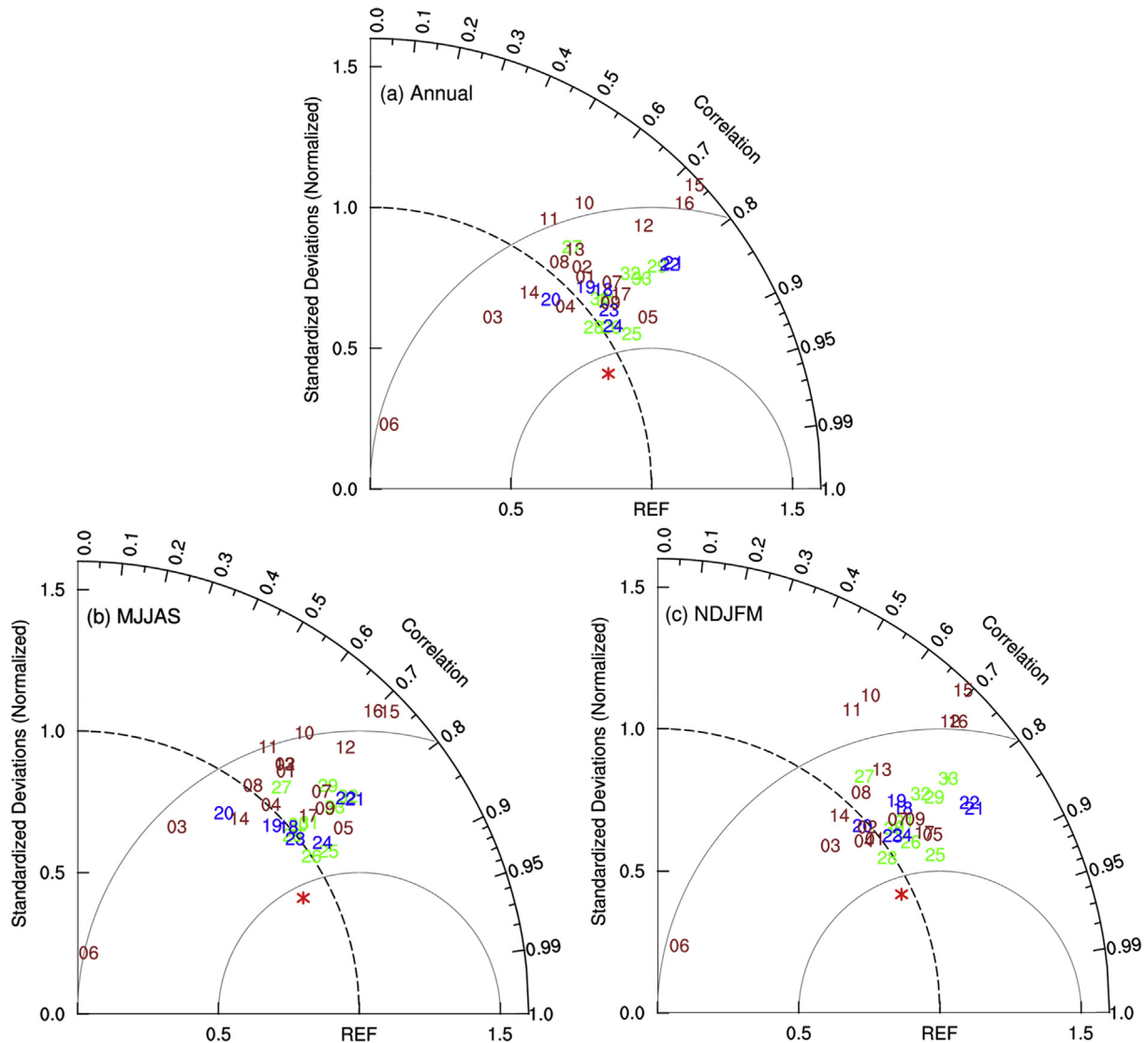


**Fig. 1.** Taylor diagram (Taylor, 2001) displaying normalised pattern statistics of climatological (a) Annual, (b) May–September, and (c) November–March precipitation at  $40^{\circ}\text{S} - 70^{\circ}\text{N}$  between each of 33 models for the reference period and observation for 1979–2000. Each number represents a Model ID (see Table 1); brown, blue, and green represent PMIP1, PMIP2, and PMIP3 models, respectively; the red asterisk represents the arithmetic mean of the 17 models finally chosen for analysis; and observation is regarded as the reference (REF). The standard deviation and centred root-mean-square difference are normalised by the observed standard deviation. The radial distance from the origin is the normalised standard deviation of a model; the spatial correlation coefficient between a model and the reference is expressed by the azimuthal position of the model; and the normalised centred root-mean-square difference between a model and the reference is their distance apart. (For interpretation of the references to colour in this figure legend, the reader is referred to the web version of this article.)

decreased over the oceans (Fig. 3b–c) on the basis of the LGM land–sea distribution reconstructed by Peltier (2004). This is mainly because some coastal ocean monsoon areas at the reference period changed to land monsoon areas at the LGM due to a sea level fall of approximately 125 m (Peltier, 2004). In fact, if we only consider the present land area, global land monsoon areas decreased in most models and by an average of 5.8%.

In the northern hemisphere, the northern boundary of land monsoon areas generally retreated southward, while their southern boundary expanded southward (Fig. 4), consistent with a southward shift of boreal wetlands (Weber et al., 2010). Monsoon areas shrank over the tropical western North Pacific and expanded over the tropical central North Pacific. In the southern hemisphere, the northern boundary of land monsoon areas generally retreated southward over southern Africa and South America but expanded northward over Indonesia and Papua New Guinea, while their southern boundary varied very little. Monsoon areas obviously

expanded northward over the Southeast Asian seas, but shrank over the southwestern tropical Indian Ocean where model agreement is low. For all models together, the LGM monsoon area varied by 4.4% and 12.1% (–2.5% and –53.3%) for the boreal and austral land (ocean), respectively. Thus, the LGM monsoon area changes shared the same sign between the boreal and austral land or ocean but the opposite signs between the land and ocean in the same hemisphere. The reduction of the GMA was a result of the decreased ocean monsoon areas in both hemispheres. Regionally, the land monsoon areas generally decreased in northern Africa, southern Africa, and South America, while most models reproduced an expansion in Asia, North America, and northern Australia.

To understand the reason underlying the LGM GMA reduction, we examined area-averaged changes in summer–minus–winter, summer, and annual precipitation over regions where the LGM monsoon area differed from the reference period. Globally, the former variable varied little. Of importance is that the reduction of

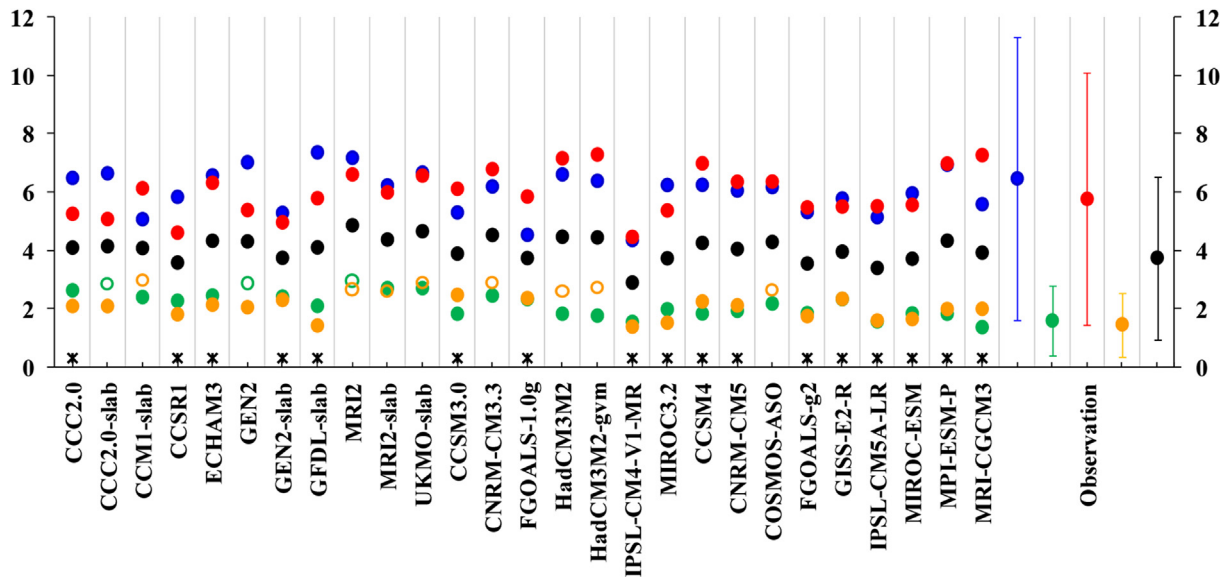


**Fig. 2.** Area-averaged precipitation (units:  $\text{mm day}^{-1}$ ) obtained from each reference experiment of 27 models and from observation for May–September (blue) and November–March (green) in the boreal monsoon area, for November–March (red) and May–September (orange) in the austral monsoon area, and for the annual mean in the GMA (black). Open circles denote the simulated values being beyond the range of  $\pm 75\%$  deviations from the corresponding observed values as expressed by vertical bars. The black asterisk above the abscissa indicates each of the 17 models finally chosen for analysis. (For interpretation of the references to colour in this figure legend, the reader is referred to the web version of this article.)

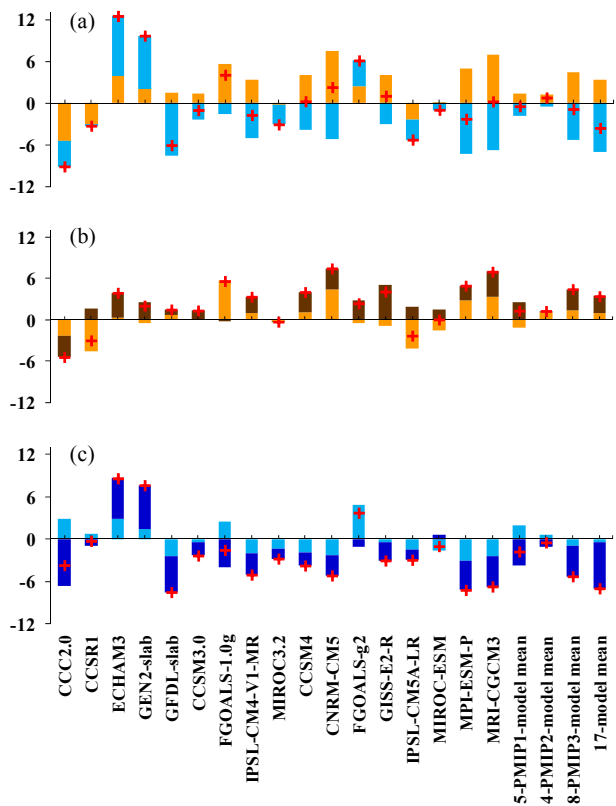


**Fig. 3.** Changes of monsoon area (units:  $10^6 \text{ km}^2$ ) in the LGM relative to the reference period: (a) the globe (red plus) and global land (orange bar) and ocean (light blue bar) area; (b) the global (red plus) and northern (orange bar) and southern (brown bar) hemispheric land; and (c) the global (red plus) and northern (light blue bar) and southern (dark blue bar) hemispheric ocean. (For interpretation of the references to colour in this figure legend, the reader is referred to the web version of this article.)

summer precipitation was larger than or comparable to that of annual precipitation, hence the ratio of summer to annual precipitation decreased and in turn led to a decrease in GMA. Over the LGM-changed global land monsoon area that included a small part of ocean monsoon areas at the reference period due to the sea level fall, both the summer precipitation deficit and the summer to annual precipitation ratio reduction contributed to the land monsoon area changes. Over the LGM-changed global ocean monsoon area, summer-minus-winter precipitation was little varied, and the summer to annual precipitation ratio generally decreased. Altogether, the reduction of the GMA and global ocean monsoon area resulted from the decreased summer to annual precipitation ratio, and both the reduction in the summer-minus-winter precipitation and the summer to annual precipitation ratio were responsible for global land monsoon area changes at the LGM.

4.2. LGM global monsoon precipitation

Compared to the reference period, the GMP decreased on average by 8.9%. More land and less ocean monsoon precipitation occurred globally (Fig. 5a), which was mainly because when more continental shelves were exposed due to the LGM sea level fall, a considerable amount of coastal ocean monsoon precipitation at the reference period changed to the land type. Geographically, the LGM monsoon precipitation changes were spatially consistent among the three groups of PMIP1, PMIP2, and PMIP3 models, as well as their arithmetic mean (Fig. 6a–d). Monsoon precipitation generally decreased over the boreal land, the northern part of southern Africa, and much of South America, increased over the southern part of southern Africa, and varied slightly over northern Australia. Ocean monsoon precipitation generally increased over part of the tropical western North Pacific, the Indian Ocean around Madagascar, and part of the tropical central South Pacific, but decreased over the Bay of Bengal, the South China Sea, and tropical northern Atlantic Ocean. Comparatively, both the sign and magnitude of the changes in ocean monsoon precipitation were similar between PMIP2 and PMIP3 models, except over the Bay of Bengal

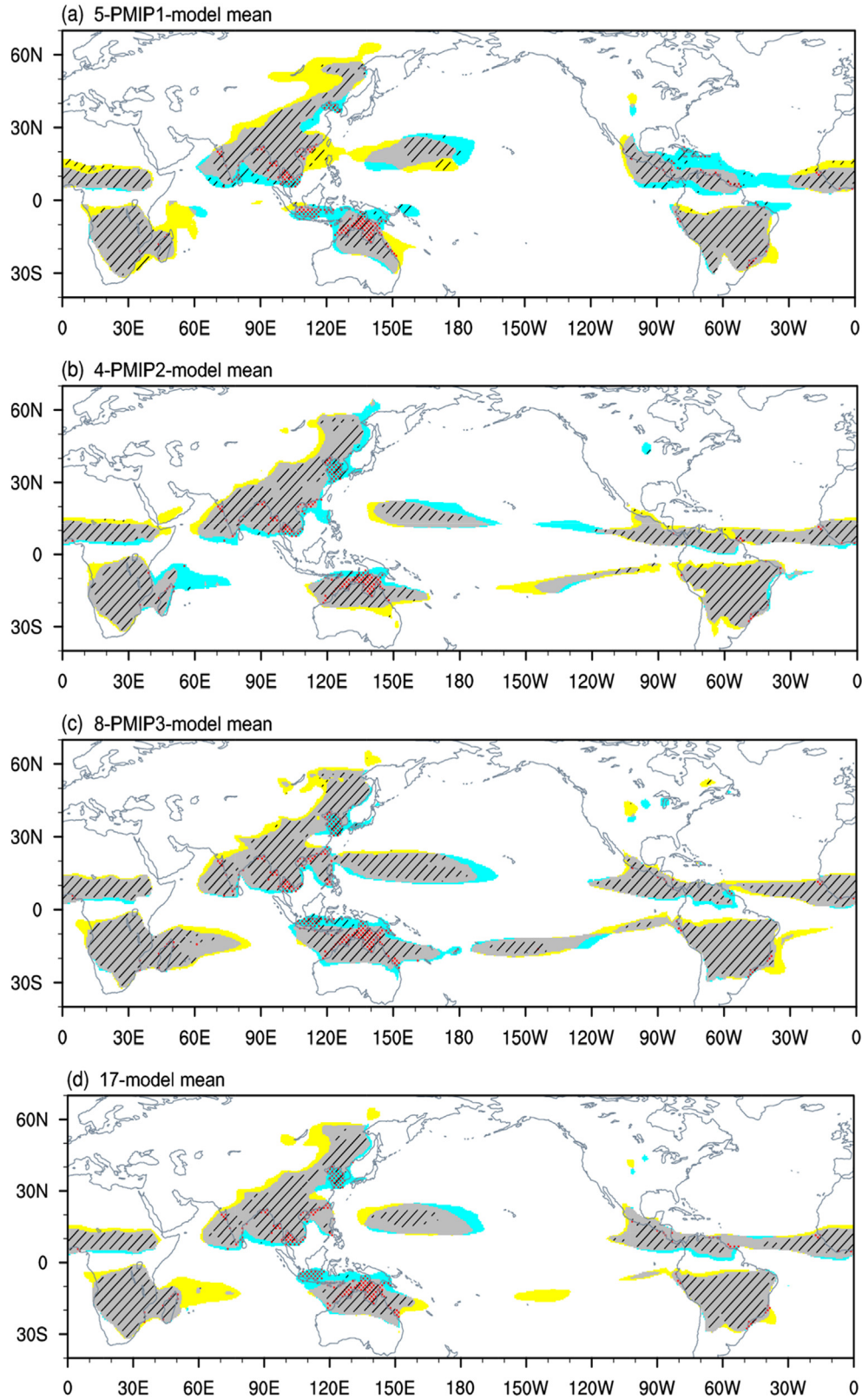


**Fig. 4.** Global monsoon area for the arithmetic means of (a) five PMIP1, (b) four PMIP2, (c) eight PMIP3, and (d) all 17 models. Grey indicates the common area between the LGM and the reference period; blue (yellow) indicates expanded (reduced) monsoon area; and red dots indicate increased land area due to the LGM sea level fall relative to the reference period. The hatched areas represent regions where at least 60% of the models agree on the signal. (For interpretation of the references to colour in this figure legend, the reader is referred to the web version of this article.)

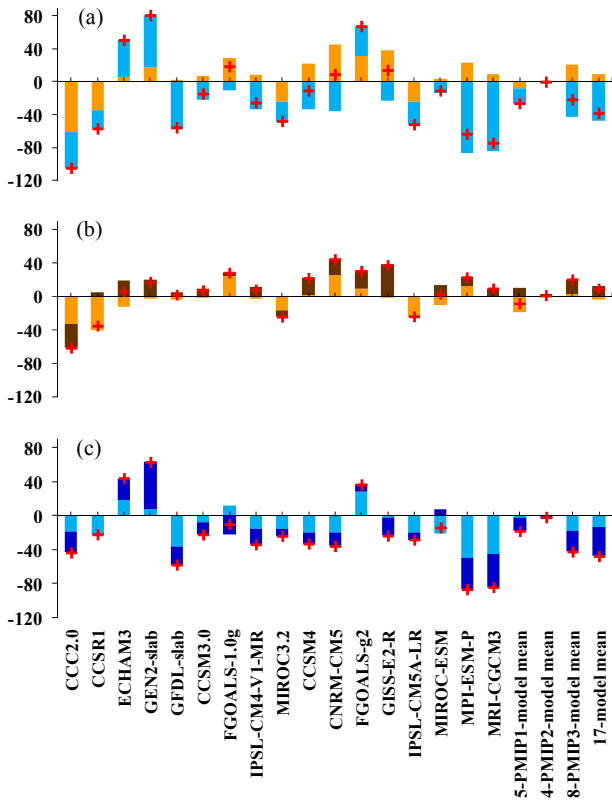


**Fig. 5.** Changes of monsoon precipitation (units:  $10^9 \text{ m}^3 \text{ day}^{-1}$ ) in the LGM relative to the reference period: (a) the globe (red plus) and global land (orange bar) and ocean (light blue bar); (b) the global (red plus) and northern (orange bar) and southern (brown bar) hemispheric land; and (c) the global (red plus) and northern (light blue bar) and southern (dark blue bar) hemispheric ocean. (For interpretation of the references to colour in this figure legend, the reader is referred to the web version of this article.)

where more monsoon precipitation appeared in PMIP2 models but less in PMIP3 models. Also of note is that ocean monsoon precipitation varied less in coupled models overall than in atmospheric models, indicative of a suppressing effect of the dynamic ocean.

At the hemispheric scale, the decreased GMP was derived from the deficit over the oceans and the boreal land, while the increased land monsoon precipitation came from the southern hemisphere (Fig. 5b–c). Monsoon precipitation changes were qualitatively consistent among individual models for regional land monsoon areas (Fig. 6a–d). Less monsoon precipitation appeared for northern Africa, Asia, North America, northern part of southern Africa, and South America, but more for southern part of southern Africa and northern Australia. The aforementioned increase in the austral land monsoon precipitation mainly stemmed from northern Australia.

#### 4.3. LGM global monsoon precipitation intensity

Taking into account the above changes in both GMA and GMP, the LGM GMPI weakened by 4.3% against the reference period. Similar magnitudes of weakening occurred for the global land and ocean monsoon areas. At the hemispheric scale, the intensity of monsoon precipitation decreased for the boreal land and ocean as well as the austral land. For the austral ocean, monsoon precipitation strengthened in four of five PMIP1 models and weakened in eight of 12 PMIP2/3 models. This resulted mainly from the increased (decreased) intensity over the southwestern tropical Indian Ocean (Fig. 6a–c) due to lower-tropospheric convergence

(divergence) associated with large-scale changes in sea surface temperatures in the former (latter), indicative of an effect of the dynamic ocean. The LGM changes in the land monsoon precipitation intensity are generally consistent in direction among individual models, since most of them simulated a weakening in northern Africa, Asia, North America, southern Africa, and South America but a strengthening in northern Australia (Fig. 6a–d). Quantitatively, those changes differed in magnitude between regions, with larger values in North America and northern Australia and smaller ones in southern Africa.

#### 4.4. Relationship among the LGM changes in GMA, GMP, and GMPI

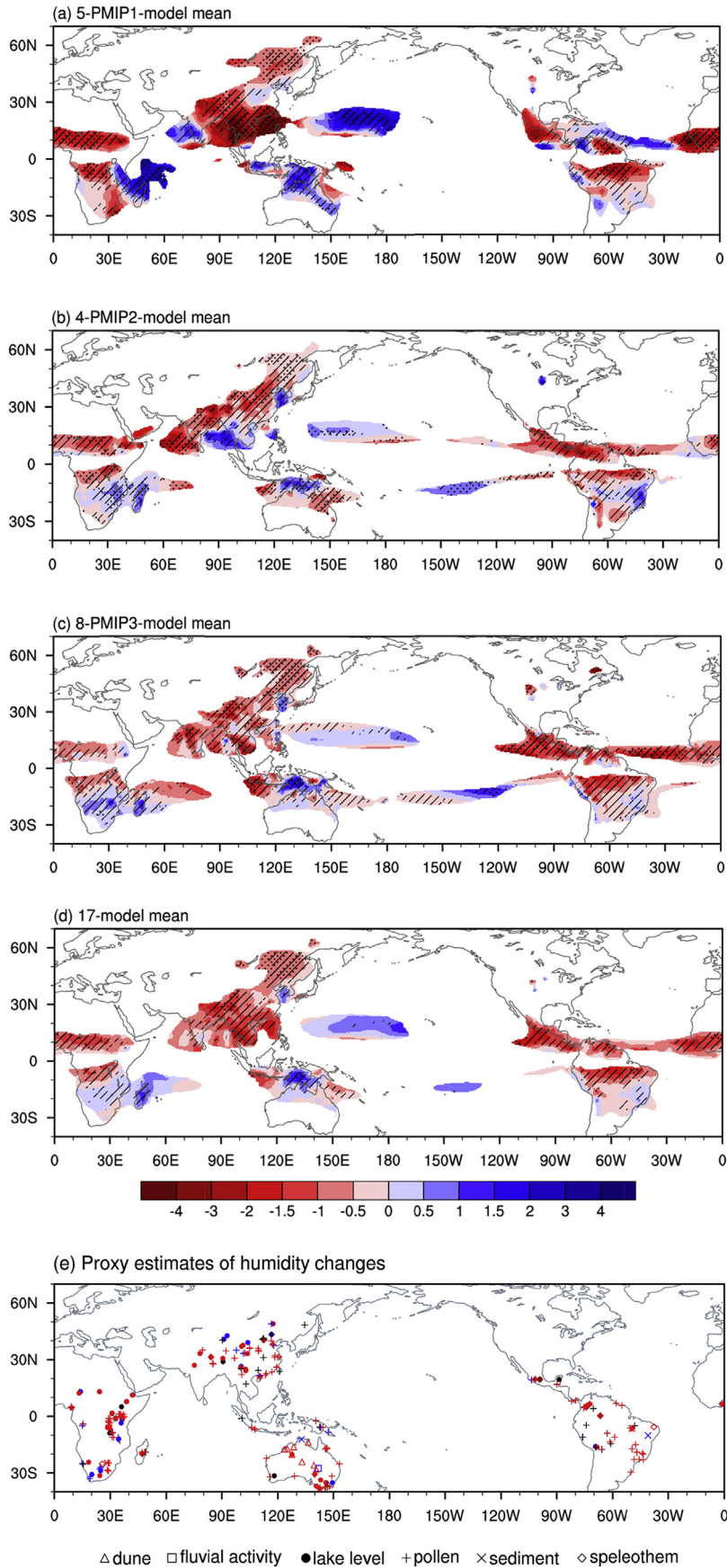
Based on the individual models and their arithmetic mean, Fig. 7 illustrates that there are positive correlations between the LGM changes in GMA ( $\Delta\text{GMA}$ ), GMP ( $\Delta\text{GMP}$ ), and GMPI ( $\Delta\text{GMPI}$ ). The correlation coefficient reaches 0.89 between  $\Delta\text{GMP}$  and  $\Delta\text{GMA}$  and 0.81 between  $\Delta\text{GMP}$  and  $\Delta\text{GMPI}$ , both of which were statistically significant at the 99.9% confidence level. As deduced from the following formulae,  $\Delta\text{GMP}$  can be expressed as the sum of three terms: monsoon precipitation change over the LGM-increased monsoon area ( $\text{GMA}_{\text{lgm-com}} \times \text{GMPI}_{\text{lgm}}$ );  $\Delta\text{GMPI}$ -induced monsoon precipitation change over the common monsoon area between the LGM and the reference period ( $\text{GMA}_{\text{com}} \times \Delta\text{GMPI}$ ); and monsoon precipitation change over the LGM-decreased monsoon area ( $-\text{GMA}_{\text{ref-com}} \times \text{GMPI}_{\text{ref}}$ ). In this context,  $\Delta\text{GMP}$  was correlated positively with  $\Delta\text{GMA}$  indirectly through  $\text{GMA}_{\text{lgm-com}}$  and with  $\Delta\text{GMPI}$  directly. More specifically, the first term was  $58.5\text{--}203.7 \times 10^9 \text{ m}^3 \text{ day}^{-1}$ ; the second term ranged from  $-3.5 \times 10^9 \text{ m}^3 \text{ day}^{-1}$  to  $-67.4 \times 10^9 \text{ m}^3 \text{ day}^{-1}$  for 14 models, and was slightly positive for the remaining three models; and the third term ranged from  $-60.8 \times 10^9 \text{ m}^3 \text{ day}^{-1}$  to  $-209.9 \times 10^9 \text{ m}^3 \text{ day}^{-1}$ . Therefore, the LGM GMP deficit was due to, first, the GMA reduction and, second, the GMPI weakening. In addition,  $\Delta\text{GMA}$  was related to  $\Delta\text{GMPI}$  indirectly, with a correlation coefficient of 0.49 (statistically significant at the 95.6% confidence level). In general, the smaller  $\Delta\text{GMA}$  was, the smaller  $\Delta\text{GMPI}$  was, and vice versa.

$$\begin{aligned}
 \Delta\text{GMP} &= \text{GMP}_{\text{lgm}} - \text{GMP}_{\text{ref}} \\
 &= \text{GMA}_{\text{lgm}} \times \text{GMPI}_{\text{lgm}} - \text{GMA}_{\text{ref}} \times \text{GMPI}_{\text{ref}} \\
 &= (\text{GMA}_{\text{lgm-com}} + \text{GMA}_{\text{com}}) \times \text{GMPI}_{\text{lgm}} - (\text{GMA}_{\text{ref-com}} \\
 &\quad + \text{GMA}_{\text{com}}) \times \text{GMPI}_{\text{ref}} \\
 &= \text{GMA}_{\text{lgm-com}} \times \text{GMPI}_{\text{lgm}} + \text{GMA}_{\text{com}} \times (\text{GMPI}_{\text{lgm}} \\
 &\quad - \text{GMPI}_{\text{ref}}) - \text{GMA}_{\text{ref-com}} \times \text{GMPI}_{\text{ref}} \\
 &= \text{GMA}_{\text{lgm-com}} \times \text{GMPI}_{\text{lgm}} + \text{GMA}_{\text{com}} \times \Delta\text{GMPI} \\
 &\quad - \text{GMA}_{\text{ref-com}} \times \text{GMPI}_{\text{ref}}
 \end{aligned}$$

where  $\Delta$  denotes the LGM minus reference, and subscripts lgm, ref, and com denote the LGM, the reference period, and the common monsoon area between the LGM and the reference period, respectively.

#### 4.5. Dynamic mechanism for the LGM monsoon area and precipitation changes

It has been well documented that the LGM cooling was resulted from relatively well-defined radiative perturbations, linked to large ice sheets and lower atmospheric concentrations of greenhouse gases, and was modified by internal feedbacks of the climate



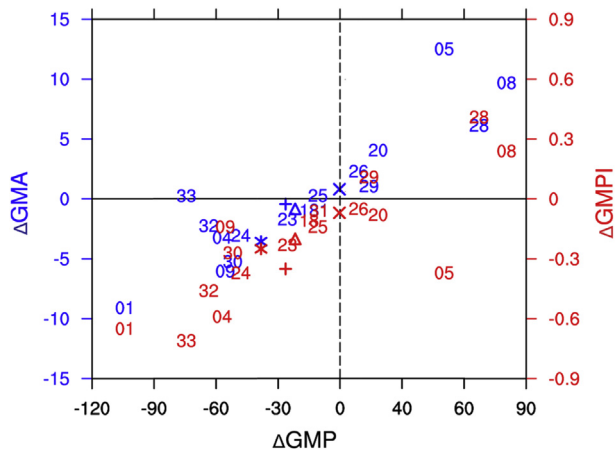


**Fig. 7.** Relative to the reference period, the LGM changes of GMP ( $\Delta\text{GMP}$ , units:  $10^9 \text{ m}^3 \text{ day}^{-1}$ ), GMA ( $\Delta\text{GMA}$ , blue, units:  $10^6 \text{ km}^2$ ), and GMPI ( $\Delta\text{GMPI}$ , red, units:  $\text{mm day}^{-1}$ ). Each number represents a Model ID (see Table 1), and plus, cross, triangle, and asterisk represent the arithmetic means of (a) five PMIP1, (b) four PMIP2, (c) eight PMIP3, and (d) all 17 models, respectively. (For interpretation of the references to colour in this figure legend, the reader is referred to the web version of this article.)

system from such as snow, sea-ice, and water vapour (e.g., Braconnot et al., 2007; Masson-Delmotte et al., 2013). Fig. 8a–b shows that summer 2-m air temperature reduced significantly relative to the reference period. In the northern hemisphere, surface cooling generally amplified northward due to, in particular, the albedo and high altitude of the ice sheets and sea ice at the high-latitudes. The summer meridional temperature gradient consequently increased for latitudes ranging from  $0^\circ$  to  $70^\circ\text{N}$  (Figs. 8 and 9a), leading to anomalous northerly winds that brought relatively dry and cold air from the high-latitudes in the lower troposphere. As a result, southerly winds and moisture transport from the tropics were suppressed at the low- and mid-latitudes, as already seen in the simulated weakening of low-tropospheric winds in West Africa (Braconnot et al., 2000), the Arabian Sea (Shin et al., 2003), southern Asia (Prell and Kutzbach, 1987), and East Asia (Yanase and Abe-Ouchi, 2007; Zhou and Zhao, 2009; Jiang and Lang, 2010). At the same time, surface cooling was stronger over land than over the oceans, leading to a decreased land–sea thermal contrast, particularly at the mid- and high-latitudes (Fig. 8a and Fig. 9c). At  $0^\circ$ – $70^\circ\text{N}$ , summer temperature reduced by  $7.3^\circ\text{C}$  over land and  $3.3^\circ\text{C}$  over the oceans for all models. Consequently, winds and moisture transport from the oceans towards the land were largely suppressed in the lower troposphere. The anomalous water vapour flux generally diverged in the land monsoon areas, while the anomalous convergence explained the increased monsoon precipitation over the tropical western North Pacific (Fig. 6c and Fig. 10a).

In the southern hemisphere, summer temperature reduced between  $0^\circ$  and  $40^\circ\text{S}$  and at similar magnitude across the latitudinal range, and in turn meridional temperature gradient was little varied (Figs. 8 and 9b). However, the zonal mean of the large-scale land–sea thermal contrast decreased (Fig. 9c). Particularly, surface cooling was stronger over southern Africa, Australia, and South America than over the surrounding oceans (Fig. 8b). At  $0^\circ$ – $40^\circ\text{S}$ , area-averaged summer temperature decreased by  $2.8^\circ\text{C}$

over land and  $1.8^\circ\text{C}$  over the oceans for all models. Accordingly, winds and moisture transport towards the land were weakened. The anomalous water vapour divergence and convergence generally occurred in regions where monsoon precipitation decreased and increased, respectively (Fig. 6c and Fig. 10a).

In addition, it should be recalled that the LGM sea surface temperatures are prescribed to the values from CLIMAP Project Members (1981) in PMIP1 atmospheric models and are simulated by the PMIP1 slab ocean models or the PMIP2/3 oceanic general circulation models in coupled models. Compared to the reference period, the reconstructed sea surface temperatures by CLIMAP Project Members (1981) are lower over most of the global ocean except over parts of the tropical and mid-latitude oceans, while the simulated values are consistently lower over the global ocean during the LGM summer (Fig. 8c–d). Both the reconstructions (excluding warmer ocean areas) and simulations are qualitatively comparable to the recent MARGO estimate at the large scale (MARGO Project Members, 2009; Otto-Bliesner et al., 2009). These lower sea surface temperatures suppressed surface evaporation over the oceans, while lower terrestrial surface temperature (Fig. 8a–b) suppressed surface evapotranspiration over land. Averaged across 14 models with data available, the summer surface evaporation reduced on average by 7.7% for the globe and by 7.6% for the GMA. Therefore, the water vapour flux from the Earth's surface into the atmosphere was reduced. Besides, the LGM global cooling was not limited to the surface but extended into the upper troposphere. The simulated global summer temperature by eight PMIP3 models decreased on average by  $4.3$ – $5.5^\circ\text{C}$  at eight levels between 1000 hPa and 300 hPa. Such a tropospheric cooling decreased the amount of atmospheric water vapour through its inhibition on the water holding capacity of the atmosphere according to the Clausius–Clapeyron relation. During the LGM summer, the vertically integrated water vapour content from the Earth's surface to 300 hPa was notably lower than the reference period (Fig. 10b) and reduced by 39.1% for the globe and by 35.0% for the GMA based on eight PMIP3 models. Therefore, the surface and tropospheric cooling was unfavourable for global-scale monsoon area and precipitation.

#### 4.6. Qualitative model–data comparison for the LGM over land monsoon areas

The proxy data used for comparison with simulations are mainly composed of the records of dune, fluvial activity, lake level, pollen, sediment, and speleothem at 258 sites over and nearby the global land monsoon areas (Fig. 6e). Note that those reconstructions generally provide site-scale qualitative information about climatological annual precipitation and/or humidity, while simulations of land monsoon areas and precipitation mainly give large-scale quantitative information regarding summer precipitation. Since summer precipitation accounts for at least 55% of annual total precipitation (see Section 2.2) in monsoon areas, it is feasible to perform a qualitative comparison to assess consistency between simulations and reconstructions over land monsoon areas under the framework of the present land–sea mask.

For northern Africa, both the monsoon area and precipitation decrease, and most models simulate a southward retreat

**Fig. 6.** Relative to the reference period, the LGM changes of May–September (November–March) precipitation in the northern (southern) hemisphere (shading, units:  $\text{mm day}^{-1}$ ) over the GMA as shown in Fig. 4 for the arithmetic means of (a) five PMIP1, (b) four PMIP2, (c) eight PMIP3, and (d) all 17 models. In panels (a) to (d), the dotted areas represent regions where the absolute value of the multi-model mean change is larger than one standard deviation of the models, and the hatched areas represent regions where at least 60% of the models agree on the sign of the change. (e) Proxy estimates of humidity changes at 258 sites during the LGM relative to the reference period, in which red, black, and blue represent drier, normal, and wetter conditions, respectively (see Supplementary Table S1 for details and references of the records). (For interpretation of the references to colour in this figure legend, the reader is referred to the web version of this article.)

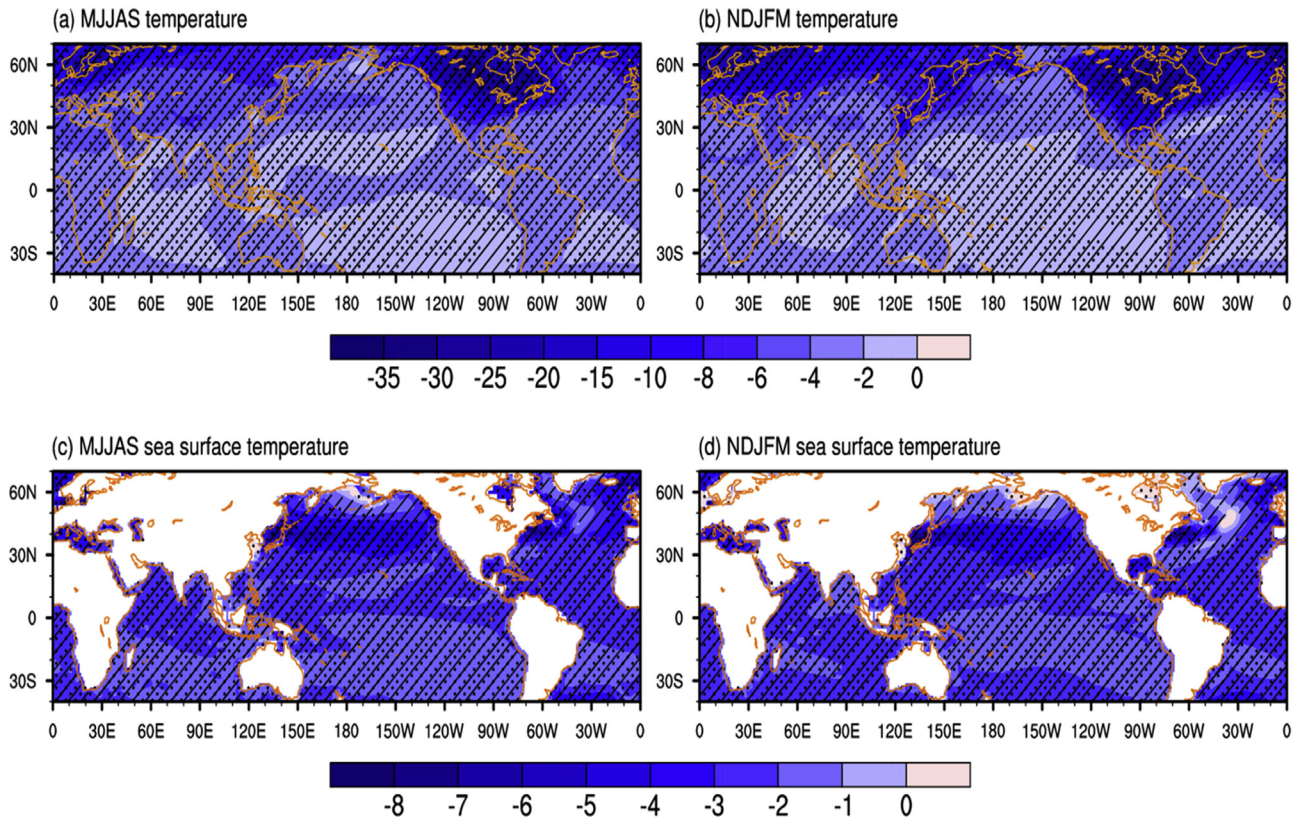


**Fig. 8.** Relative to the reference period, the LGM changes of May–September and November–March 2-m air temperatures (units: °C) from all 17 models and of sea surface temperatures (units: °C) from nine PMIP2/3 coupled models with data available. The dotted areas represent regions where the absolute value of the multi-model mean change is larger than one standard deviation of the models, and the hatched areas represent regions where at least 60% of the models agree on the sign of the change. (For interpretation of the references to colour in this figure legend, the reader is referred to the web version of this article.)

(advance) of the northern (southern) boundary of the monsoon area (Figs. 4 and 6d), averaging  $1.3^\circ$  ( $0.8^\circ$ ) between  $20^\circ\text{W}$  and  $41^\circ\text{E}$  ( $8^\circ\text{E}$  and  $40^\circ\text{E}$ ). Based on pollen data, both annual and July precipitation decrease in part of northern Africa (Wu et al., 2007), which is consistent with simulations. Drier climate is also recorded in pollen and plant macrofossil data in equatorial eastern northern Africa (Farrera et al., 1999; Bartlein et al., 2011) and in paleohydrological data of lake level, ground water, and speleothem in much of northern Africa (Gasse, 2000), and is inferred from a lowering of montane vegetation belts and a reduction of tropical moist forests in northern Africa (Jolly et al., 1998; Prentice et al., 2000). For Asia, the monsoon area and precipitation reductions, as well as a southeastward shift of the monsoon area (Figs. 4 and 6d), agree with generally lower lake levels across monsoonal Asia (Qin and Yu, 1998; Li and Morrill, 2013), strong shifts of temperate xerophytic shrubland, temperate grassland, and desert to the south and east in northern China (Yu et al., 2000; Ni et al., 2010), and an activation of aeolian dunes in the sandy lands in the eastern Chinese desert belt (Yang and Scuderi, 2010). Moreover, the simulations of the northern African and Asian monsoons support less precipitation in most of the Afro-Asian arid/semi-arid transitional zone and a southward shift of several hundred kilometres in the arid or semi-arid zones between 21,000 and 15,000 years ago as obtained from a large number of geological records (Yan and Petit-Maire, 1994). The North American monsoon area increases due to its southward advance (Fig. 4d) by an average of  $1.6^\circ$  between  $55^\circ\text{W}$  and  $77^\circ\text{W}$ , while the monsoon precipitation decreases (Fig. 6d). The latter is in accord with a dry environment, as derived from pollen and plant

macrofossil data (Farrera et al., 1999; Marchant et al., 2009).

In the southern hemisphere, most models simulate a southward (northward) retreat of the northern (southern) boundary of the southern African monsoon area (Fig. 4d), averaging  $1.0^\circ$  ( $0.2^\circ$ ) between  $13^\circ\text{E}$  and  $36^\circ\text{E}$  ( $12^\circ\text{E}$  and  $40^\circ\text{E}$ ), while monsoon precipitation decreases (increases) in the northern (southern) part of southern Africa (Fig. 6d). Comparatively, both annual and July precipitation, as well as the actual to potential evapotranspiration ratio, decreases in much of the eastern part of low-latitude southern Africa, and annual precipitation is estimated to be approximately 200 to 1000 mm lower in the equatorial region based on pollen data using inverse vegetation modelling (Wu et al., 2007) and at least 200 mm lower in the eastern part of low-latitude southern Africa based on pollen and plant macrofossil data (Bartlein et al., 2011). Evidence of a drier climate here also comes from records of lake level, ground water, and speleothem (Jolly et al., 1998; Farrera et al., 1999; Gasse, 2000) and from a lowering of montane vegetation belts and a reduction of tropical moist forests (Jolly et al., 1998; Prentice et al., 2000), while the monsoon is inferred to be weakened in subtropical southern Africa through the sedimentary record of the Pretoria Saltpan (Partridge et al., 1997). In the southern part of southern Africa, however, drier, wetter, normal conditions are registered at nine, seven, and one site (Fig. 6e), respectively, based on the records of lake level, pollen, sediment, and speleothem (Partridge et al., 1997; Farrera et al., 1999; Gasse, 2000; Wu et al., 2007; Bartlein et al., 2011).

There is uncertainty among the models regarding the northern Australian monsoon precipitation change, with a general increase (decrease) in the western (eastern) part (Fig. 6d). The wetter climate in the west is only supported by the stratigraphic data of

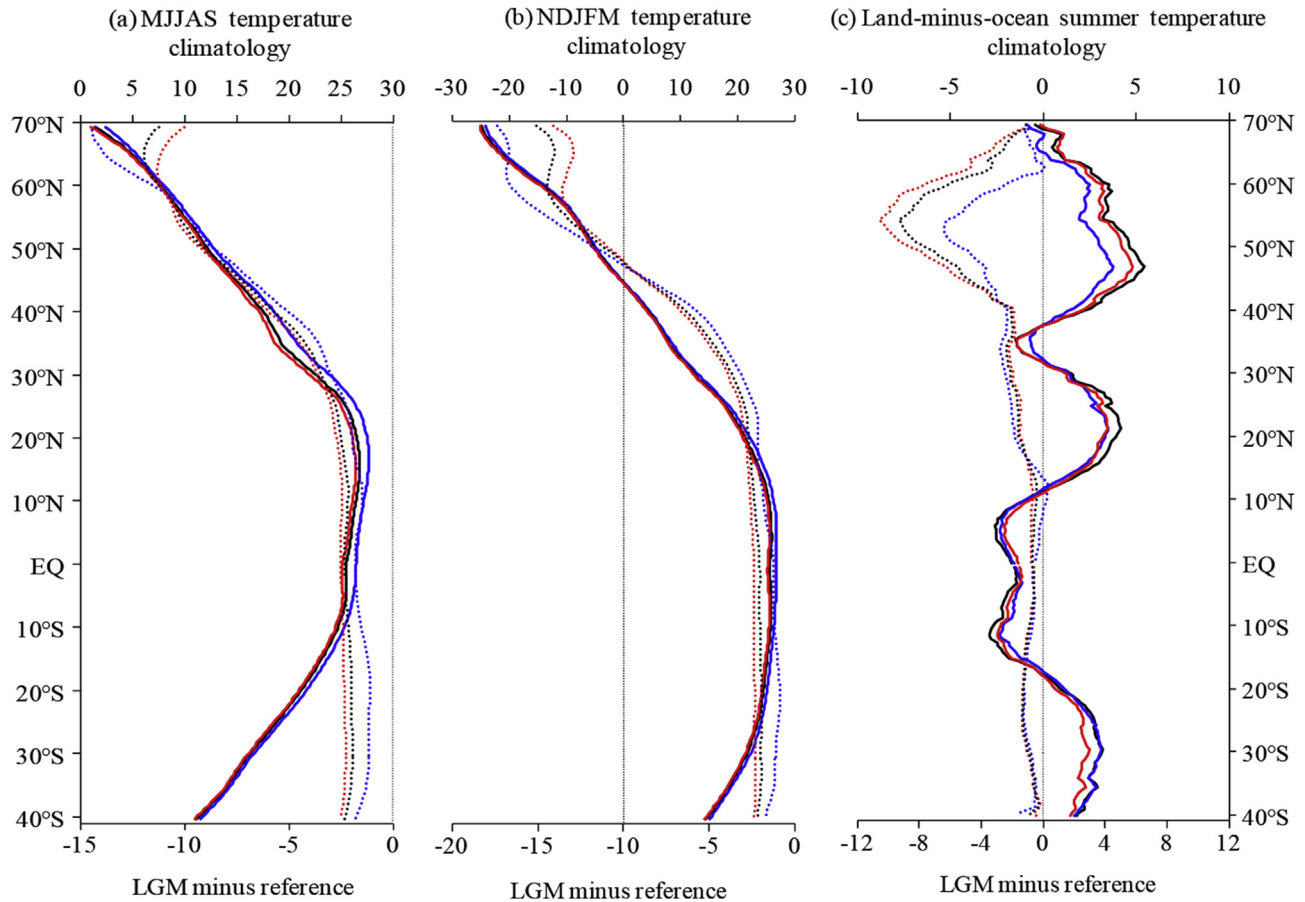


**Fig. 9.** Zonal mean of 2-m air temperature (units: °C) for (a) May–September and (b) November–March, as well as (c) zonally averaged difference in 2-m air temperature between land and ocean during May–September in the northern hemisphere and November–March in the southern hemisphere. Solid lines represent the reference period climatology (upper scales); the dotted lines represent LGM minus reference (lower scales); and blue, red, and black lines represent the arithmetic means of five PMIP1 models, 12 PMIP2/3 coupled models, and all 17 models, respectively. (For interpretation of the references to colour in this figure legend, the reader is referred to the web version of this article.)

plunge pool deposits at the Kakadu National Park that is speculated to have resulted from a strengthening of the northwest monsoon (Nott and Price, 1994). In contrast, widespread aridity in Australia is evidenced by:

- Lake and river records, more sparse vegetation, and more active sand dunes (Hesse et al., 2004)
- Extensive desert dune activity and dust transport, lake level fall, and reduced but episodic fluvial activity (Fitzsimmons et al., 2013)
- A synthesis of pollen and terrestrial sedimentary data in most lowland regions of tropical Australasia (Reeves et al., 2013)
- The expansion of xerophytic vegetation in the south and tropical deciduous broadleaf forest and woodland in the north and the

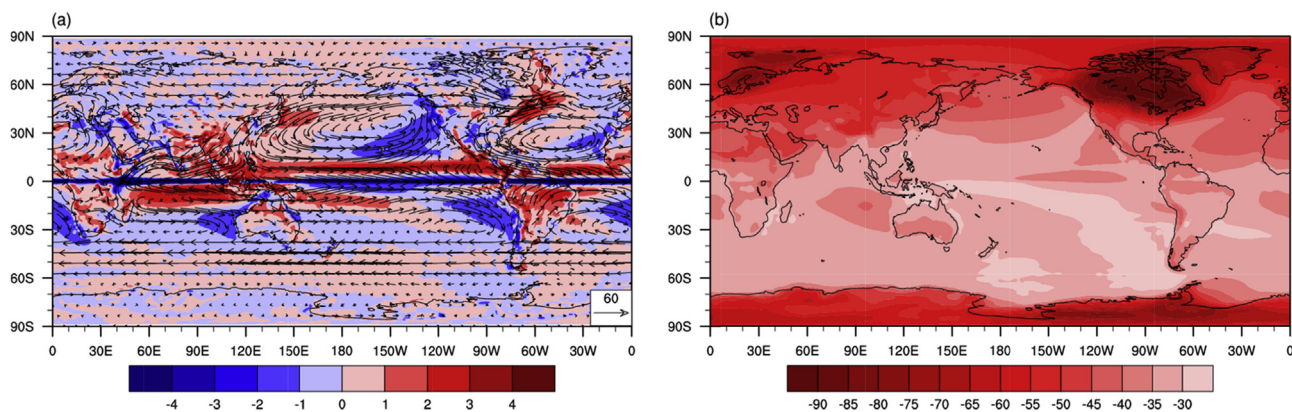


**Fig. 10.** Relative to the reference period, the LGM changes of summer (May–September in the northern hemisphere and November–March in the southern hemisphere) vertically integrated (a) water vapour flux (arrows; units:  $\text{kg m}^{-1} \text{s}^{-1}$ ) and its divergence (shading, units:  $\text{mm day}^{-1}$ ) as well as (b) water vapour content (units: %) obtained from eight PMIP3 models. The vertical integration is performed from the surface to 300 hPa. (For interpretation of the references to colour in this figure legend, the reader is referred to the web version of this article.)

encroachment of tropical deciduous broadleaf forest and woodland into lowland evergreen broadleaf forest (Pickett et al., 2004).

The monsoon is considered to be inactive or greatly weakened at that time (Hesse et al., 2004; Reeves et al., 2013).

Most models simulate a southward (northward) retreat of the northern (southern) boundary of the South American monsoon area (Fig. 4d), averaging  $0.9^\circ$  ( $0.2^\circ$ ) between  $36^\circ\text{W}$  and  $81^\circ\text{W}$  ( $38^\circ\text{W}$  and  $78^\circ\text{W}$ ), while monsoon precipitation decreases (Fig. 6d). On the one hand, there is evidence that the Amazon was somewhat drier in glacial times, a concept given substance by pollen data for the movement of ecotones in Rondonia, by stream histories in the Bolivian Andes, by evidence for lowered lake levels at Carajas and Lake Pata, and by a sedimentary hiatus at Carajas (Colinvaux et al., 2000; Sifeddine et al., 2001). Speleothem records indicate predominantly dry conditions at the Rio Grande do Norte of northeastern Brazil (Cruz et al., 2009). Plant available moisture decreases in much of South America based on pollen and plant macrofossil data (Farrera et al., 1999). On the other hand, long sediment cores from the deep portions of Lake Titicaca reveal a deep, fresh, and continuously overflowing lake between 25,000 and 15,000 years ago, signifying that the Altiplano of Bolivia and Peru and much of the Amazon basin were wetter than today (Baker et al., 2001). Speleothem records and travertine deposits in northern Bahia State of northeastern Brazil indicate that wet periods were synchronous with cold periods in Greenland over the past 210,000 years (Wang et al., 2004).

Altogether, model–reconstruction comparison demonstrates qualitative agreement in northern Africa, Asia, North America, the northern part of southern Africa, and the eastern part of northern Australia, but disagreement in the western part of northern Australia. It is impossible to assess the consistency between simulations and reconstructions in South America and the southern part of southern Africa, as both wetter and drier climates are suggested by multi-proxy records. When viewed from different stages of the models from PMIP1 to PMIP3, monsoon precipitation changes are broadly similar in large-scale spatial patterns, but are generally greater in atmospheric and atm–slab ocean models than in fully coupled models (Fig. 6a–c), indicative of a suppressing effect of ocean feedback upon the response of monsoon precipitation to the glacial boundary conditions. Compared to reconstructions, coupled models perform qualitatively better over much of central-eastern China and northern Australia than the earlier PMIP1 models, while PMIP2 and PMIP3 simulations are highly consistent (Fig. 6). The former signifies an improvement from PMIP1 to PMIP2, when models started to include ocean dynamics and thus interactions between oceanic and atmospheric processes. In addition, the LGM simulations do not support an orbital-scale inter-hemispheric anti-phasing of monsoon intensity change as suggested by proxy data (Masson-Delmotte et al., 2013), particularly either between the Asian and South American monsoons as seen through speleothem records (Wang et al., 2004; Cheng et al., 2012) or between the northern and southern African monsoons due to the Earth orbital precession as proposed based mainly on sedimentary records (Partridge et al., 1997). This may be explained by the opinion of Guo et al. (2012) that orbital-scale global monsoon can be regarded as a system consisting of two integrated components. One is related to the low-latitude summer insolation changes, roughly anti-phased between the two hemispheres; and the other is modulated by the glacial–interglacial cycles, mostly synchronous at the global scale. The latter component most likely dominates at the LGM because at that time orbital parameters differed minimally from the pre-industrial period (Berger, 1978) and a global-scale cooling occurred in response to large ice sheets and lower

greenhouse gas concentrations.

## 5. Conclusion

In this study, the concept of global monsoon was applied to the glacial climate during the LGM based on the experiments of 17 climate models within PMIP1/2/3. The primary conclusions are as follows.

- (1) In comparison to the reference period, the LGM monsoon area increased over land and decreased over the oceans, owing mainly to coastal ocean monsoon areas becoming land ones due to the sea level fall from the pre-industrial to LGM. The boreal land monsoon areas shifted southward, while the austral land monsoon areas contracted meridionally in southern Africa and South America but varied slightly in northern Australia. The reduction in GMA and global ocean monsoon area were related to the decreased summer to annual precipitation ratio, and both the decreased summer-minus-winter precipitation and summer to annual precipitation ratio affected global land monsoon area.
- (2) At the LGM, an 8.9% decrease of the GMP was derived from the oceans and the boreal land, and a 4.3% weakening of the GMPI from the land and the boreal ocean. There are positive correlations between the changes in GMA, GMP, and GMPI, and the GMP deficit is attributed to both the GMA reduction and the GMPI weakening, particularly the former.
- (3) In response to the LGM boundary conditions, the increased summer meridional temperature gradient in the northern hemisphere, the decreased summer land–sea thermal contrast at  $40^\circ\text{S}$ – $70^\circ\text{N}$ , and the global cooling at the surface and in the troposphere are responsible for the large-scale decrease in monsoon areas and precipitation.
- (4) Qualitatively, simulations agree with reconstructions in most of global land monsoon areas except in the western part of northern Australia where disagreements occur and in South America and the southern part of southern Africa where proxy data uncertainty exists. Coupled models perform qualitatively better over much of central-eastern China and northern Australia than the earlier PMIP1 models. The previously proposed inter-hemispheric anti-phasing either between the Asian and South American monsoons or between the northern and southern African monsoons on the orbital scale is not supported by the present analysis.

Finally, we would like to stress that the simulated LGM monsoon area and precipitation vary from model to model. This model-dependent uncertainty may arise from the difference in the experimental design of the simulations through the three phases of PMIP, from the difference in the model resolution and structure that determine their internal natural variability and their sensitivity to external perturbations, and from insufficient integration time to reach an equilibrium state for boundary conditions (Masson-Delmotte et al., 2013). Moreover, ocean and vegetation are two core components of the climate system. The present experiments of three atmospheric models, two atm–slab ocean models, and 12 fully coupled atmosphere–ocean or atmosphere–ocean–vegetation models make it impossible to detect the effect of ocean feedback on the LGM global monsoon directly through comparisons between atmospheric and coupled models, as is the dynamical vegetation that is only partly taken into account in three of 17 models, namely FGOALS-g2, IPSL-CM5A-LR, and MIROC-ESM. Both effects need to be further investigated by performing special experiments using a hierarchy of models from the same family in a transparent manner (e.g., Braconnot et al., 1999; Jahn et al., 2005).

Furthermore, still missing is dust feedback, an important process for the LGM climate (Masson-Delmotte et al., 2013). Other experiments are required to disentangle the contribution of the different LGM forcings (ice-sheets, greenhouse gases, and astronomical parameters) to the changes in monsoon described here. Therefore both climate models and the numerical experiment design need to be improved in future studies. On the other hand, it should be kept in mind that the spatial coverage of the proxy data used for the present model–data comparison is still sparse. More reconstructions using multiple proxies and methods are desired to constrain the simulations, particularly in South America and the southern part of southern Africa where large uncertainty exists.

## Acknowledgements

We sincerely thank three anonymous reviewers and the editor Xiaoping Yang for their insightful comments. We also thank the climate modelling groups (listed in Table 1) for producing and sharing their model output. This work was supported by the Strategic Priority Research Program (XDB03020602) of the Chinese Academy of Sciences and by the National Natural Science Foundation of China (41421004 and 41222034). The analyses were performed using version 10 January 2014 of the database. More information is available on <http://pmip3.lscce.ipsl.fr/>.

## Appendix A. Supplementary data

Supplementary data related to this article can be found at <http://dx.doi.org/10.1016/j.quascirev.2015.08.033>.

## References

- An, Z., Clemens, S.C., Shen, J., Qiang, X., Jin, Z., Sun, Y., Prell, W.L., Luo, J., Wang, S., Xu, H., Cai, Y., Zhou, W., Liu, X., Liu, W., Shi, Z., Yan, L., Xiao, X., Chang, H., Wu, F., Ai, L., Lu, F., 2011. Glacial-interglacial Indian summer monsoon dynamics. *Science* 333, 719–723.
- Baker, P.A., Seltzer, G.O., Fritz, S.C., Dunbar, R.B., Grove, M.J., Tapia, P.M., Cross, S.L., Rowe, H.D., Broda, J.P., 2001. The history of South American tropical precipitation for the past 25,000 years. *Science* 291, 640–643.
- Bartlein, P.J., Harrison, S.P., Brewer, S., Connor, S., Davis, B.A.S., Gajewski, K., Guiot, J., Harrison-Prentice, T.I., Henderson, A., Peyron, O., Prentice, I.C., Scholze, M., Seppä, H., Shuman, B., Sugita, S., Thompson, R.S., Viau, A.E., Williams, J., Wu, H., 2011. Pollen-based continental climate reconstructions at 6 and 21 ka: a global synthesis. *Clim. Dyn.* 37, 775–802.
- Berger, A.L., 1978. Long-term variations of daily insolation and quaternary climatic changes. *J. Atmos. Sci.* 35, 2362–2367.
- Braconnot, P., Jousaume, S., Marti, O., de Noblet, N., 1999. Synergistic feedbacks from ocean and vegetation on the African monsoon response to mid-holocene insolation. *Geophys. Res. Lett.* 26, 2481–2484.
- Braconnot, P., Jousaume, S., de Noblet, N., Ramstein, G., 2000. Mid-Holocene and last glacial maximum African monsoon changes as simulated within the paleoclimate modelling intercomparison project. *Glob. Planet. Change* 26, 51–66.
- Braconnot, P., Otto-Bliesner, B., Harrison, S., Jousaume, S., Peterchmitt, J.-Y., Abe-Ouchi, A., Crucifix, M., Driesschaert, E., Fichetef, Th, Hewitt, C.D., Kageyama, M., Kitoh, A., Loutre, M.-F., Marti, O., Merkel, U., Ramstein, G., Valdes, P., Weber, L., Yu, Y., Zhao, Y., 2007. Results of PMIP2 coupled simulations of the mid-Holocene and last glacial maximum – Part 2: feedbacks with emphasis on the location of the ITCZ and mid- and high latitudes heat budget. *Clim. Past* 3, 279–296.
- Braconnot, P., Harrison, S.P., Kageyama, M., Bartlein, P.J., Masson-Delmotte, V., Abe-Ouchi, A., Otto-Bliesner, B., Zhao, Y., 2012. Evaluation of climate models using palaeoclimatic data. *Nat. Clim. Change* 2, 417–424.
- Cheng, H., Sinha, A., Wang, X., Cruz, F.W., Edwards, R.L., 2012. The global paleomonsoon as seen through speleothem records from Asia and the Americas. *Clim. Dyn.* 39, 1045–1062.
- CLIMAP Project Members, 1981. Seasonal reconstructions of the earth's surface at the last glacial maximum. In: Geological Society of America Map Chart Series MC-36. Geol. Soc. Am, Boulder, Colorado.
- Colinvaux, P.A., De Oliveira, P.E., Bush, M.B., 2000. Amazonian and neotropical plant communities on glacial time-scales: the failure of the aridity and refuge hypotheses. *Quat. Sci. Rev.* 19, 141–169.
- Cruz, F.W., Vuille, M., Burns, S.J., Wang, X., Cheng, H., Werner, M., Edwards, R.L., Karmann, I., Auler, A.S., Nguyen, H., 2009. Orbitally driven east–west anti-phasing of South American precipitation. *Nat. Geosci.* 2, 210–214.
- Farrera, I., Harrison, S.P., Prentice, I.C., Ramstein, G., Guiot, J., Bartlein, P.J., Bonnefille, R., Bush, M., Cramer, W., von Grafenstein, U., Holmgren, K., Hooghiemstra, H., Hope, G., Jolly, D., Lauritzen, S.E., Ono, Y., Pinot, S., Stute, M., Yu, G., 1999. Tropical climates at the last glacial maximum: a new synthesis of terrestrial palaeoclimate data. I. Vegetation, lake-levels and geochemistry. *Clim. Dyn.* 15, 823–856.
- Fitzsimmons, K.E., Cohen, T.J., Hesse, P.P., Jansen, J., Nanson, G.C., May, J.H., Barrows, T.T., Haberlah, D., Hilgers, A., Kelly, T., Larsen, J., Lomax, J., Treble, P., 2013. Late quaternary palaeoenvironmental change in the Australian drylands. *Quat. Sci. Rev.* 74, 78–96.
- Gasse, F., 2000. Hydrological changes in the African tropics since the last glacial maximum. *Quat. Sci. Rev.* 19, 189–211.
- Guo, Z.T., Zhou, X., Wu, H., 2012. Glacial-interglacial water cycle, global monsoon and atmospheric methane changes. *Clim. Dyn.* 39, 1073–1092.
- Hesse, P.P., Magee, J.W., van der Kaars, S., 2004. Late quaternary climates of the Australian arid zone: a review. *Quat. Int.* 118–119, 87–102.
- Hsu, P., Li, T., Luo, J.J., Murakami, H., Kitoh, A., Zhao, M., 2012. Increase of global monsoon area and precipitation under global warming: a robust signal? *Geophys. Res. Lett.* 39 <http://dx.doi.org/10.1029/2012GL051037>. L06701.
- Huffman, G.J., Adler, R.F., Bolvin, D.T., Gu, G., 2009. Improving the global precipitation record: GPCP version 2.1. *Geophys. Res. Lett.* 36 <http://dx.doi.org/10.1029/2009GL040000>. L17808.
- Jahn, A., Claussen, M., Ganopolski, A., Brovkin, V., 2005. Quantifying the effect of vegetation dynamics on the climate of the last glacial maximum. *Clim. Past* 1, 1–7.
- Jian, Z., Huang, B., Kuhnt, W., Lin, H.L., 2001. Late quaternary upwelling intensity and East Asian monsoon forcing in the South China Sea. *Quat. Res.* 55, 363–370.
- Jiang, D., Lang, X., 2010. Last glacial maximum East Asian monsoon: results of PMIP simulations. *J. Clim.* 23, 5030–5038.
- Jiang, D., Tian, Z., Lang, X., 2015. Mid-Holocene global monsoon area and precipitation from PMIP simulations. *Clim. Dyn.* 44, 2493–2512.
- Jolly, D., Harrison, S.P., Damnati, B., Bonnefille, R., 1998. Simulated climate and biomes of Africa during the late quaternary: comparison with pollen and lake status data. *Quat. Sci. Rev.* 17, 629–657.
- Li, Y., Morrill, C., 2013. Lake levels in Asia at the last glacial maximum as indicators of hydrologic sensitivity to greenhouse gas concentrations. *Quat. Sci. Rev.* 60, 1–12.
- Liu, J., Wang, B., Ding, Q., Kuang, X., Soon, W., Zorita, E., 2009. Centennial variations of the global monsoon precipitation in the last millennium: results from ECHO-G Model. *J. Clim.* 22, 2356–2371.
- Liu, T., Ding, Z., 1998. Chinese loess and the paleomonsoon. *Annu. Rev. Earth Planet. Sci.* 26, 111–145.
- Marchant, R., Cleef, A., Harrison, S.P., Hooghiemstra, H., Markgraf, V., van Boxel, J., Ager, T., Almeida, L., Anderson, R., Baied, C., Behling, H., Berrio, J.C., Burbidge, R., Björck, S., Byrne, R., Bush, M., Duijvenvoorden, J., Flenley, J., De Oliveira, P., van Geel, B., Graf, K., Gosling, W.D., Harbele, S., van der Hammen, T., Hansen, B., Horn, S., Kuhry, P., Ledru, M.P., Mayle, F., Leyden, B., Lozano-García, S., Melief, A.M., Moreno, P., Moar, N.T., Prieto, A., van Reenen, G., Salgado-Labouriau, M., Schabitz, F., Schreve-Brinkman, E.J., Wille, M., 2009. Pollen-based biome reconstructions for Latin America at 0, 6000 and 18 000 radiocarbon years ago. *Clim. Past* 5, 725–767.
- MARGO Project Members, 2009. Constraints on the magnitude and patterns of ocean cooling at the last glacial maximum. *Nat. Geosci.* 2, 127–132.
- Masson-Delmotte, V., Schulz, M., Abe-Ouchi, A., Beer, J., Ganopolski, A., González Rouco, J.F., Jansen, E., Lambeck, K., Luterbacher, J., Naish, T., Osborn, T., Otto-Bliesner, B., Quinn, T., Ramesh, R., Rojas, M., Shao, X., Timmermann, A., 2013. In: Stocker, T.F., Qin, D., Plattner, G.K., Tignor, M., Allen, S.K., Boschung, J., Nauels, A., Xia, Y., Bex, V., Midgley, P.M. (Eds.), Information from Paleoclimate Archives. In: *Climate Change 2013: The Physical Science Basis. Contribution of Working Group I to the Fifth Assessment Report of the Intergovernmental Panel on Climate Change*. Cambridge University Press, Cambridge, United Kingdom and New York, NY, USA, pp. 383–464.
- Ni, J., Yu, G., Harrison, S.P., Prentice, I.C., 2010. Palaeovegetation in China during the late quaternary: biome reconstructions based on a global scheme of plant functional types. *Paleogeogr. Paleoclimatol. Paleocool.* 289, 44–61.
- Nott, J., Price, D., 1994. Plunge pools and paleoprecipitation. *Geology* 22, 1047–1050.
- Otto-Bliesner, B.L., Schneider, R., Brady, E.C., Kucera, M., Abe-Ouchi, A., Bard, E., Braconnot, P., Crucifix, M., Hewitt, C.D., Kageyama, M., Marti, O., Paul, A., Rosell-Melé, A., Waelbroeck, C., Weber, S.L., Weinelt, M., Yu, Y., 2009. A comparison of PMIP2 model simulations and the MARGO proxy reconstruction for tropical sea surface temperatures at last glacial maximum. *Clim. Dyn.* 32, 799–815.
- Partridge, T.C., Demenocal, P.B., Lorentz, S.A., Paiker, M.J., Vogel, J.C., 1997. Orbital forcing of climate over South Africa: a 200,000-year rainfall record from the Pretoria Saltpan. *Quat. Sci. Rev.* 16, 1125–1133.
- Peltier, W.R., 2004. Global glacial isostasy and the surface of the ice-age earth: the ICE-5G (VM2) model and GRACE. *Annu. Rev. Earth Planet. Sci.* 32, 111–149.
- Pickett, E.J., Harrison, S.P., Hope, G., Harle, K., Dodson, J.R., Kershaw, A.P., Prentice, I.C., Backhouse, J., Colhoun, E.A., D'Costa, D., Flenley, J., Grindrod, J., Haberle, S., Hassell, C., Kenyon, C., Macphail, M., Martin, H., Martin, A.H., McKenzie, M., Newsome, J.C., Penny, D., Powell, J., Raine, J.L., Southern, W., Stevenson, J., Sutra, J.P., Thomas, I., van der Kaars, S., Ward, J., 2004. Pollen-based reconstructions of biome distributions for Australia, Southeast Asia and the Pacific (SEAPAC region) at 0, 6000 and 18,000 <sup>14</sup>C yr BP. *J. Biogeogr.* 31, 1381–1444.
- Prell, W.L., Kutzbach, J.E., 1987. Monsoon variability over the past 150,000 years. *J. Geophys. Res.* 92, 8411–8425.
- Prentice, I.C., Jolly, D., BIOME 6000 participants, 2000. Mid-holocene and glacial-

- maximum vegetation geography of the northern continents and Africa. *J. Biogeogr.* 27, 507–519.
- Qin, B., Yu, G., 1998. Implications of lake level variations at 6 ka and 18 ka in mainland Asia. *Glob. Planet. Change* 18, 59–72.
- Reeves, J.M., Bostock, H.C., Ayliffe, L.K., Barrows, T.T., De Deckker, P., Devriendt, L.S., Dunbar, G.B., Drysdale, R.N., Fitzsimmons, K.E., Gagan, M.K., Griffiths, M.L., Haberle, S.G., Jansen, J.D., Krause, C., Lewis, S., McGregor, H.V., Mooney, S.D., Moss, P., Nanson, G.C., Purcell, A., van der Kaars, S., 2013. Palaeoenvironmental change in tropical Australasia over the last 30,000 years – A synthesis by the OZ-INTIMATE group. *Quat. Sci. Rev.* 74, 97–114.
- Saraswat, R., Nigam, R., Correge, T., 2014. A glimpse of the quaternary monsoon history from India and adjoining seas. *Paleogeogr. Paleoclimatol. Paleoecol.* 397, 1–6.
- Schulz, H., von Rad, U., Erlenkeuser, H., 1998. Correlation between Arabian Sea and Greenland climate oscillations of the past 110,000 years. *Nature* 393, 54–57.
- Shin, S.-I., Liu, Z., Otto-Bliesner, B., Brady, E.C., Kutzbach, J.E., Harrison, S.P., 2003. A simulation of the last glacial maximum climate using the NCAR-CCSM. *Clim. Dyn.* 20, 127–151.
- Sifeddine, A., Martin, L., Turcq, B., Volkmer-Ribeiro, C., Soubiès, F., Cordeiro, R.C., Suguio, K., 2001. Variations of the Amazonian rainforest environment: a sedimentological record covering 30,000 years. *Paleogeogr. Paleoclimatol. Paleoecol.* 168, 221–235.
- Taylor, K.E., 2001. Summarizing multiple aspects of model performance in a single diagram. *J. Geophys. Res.* 106 (D7), 7183–7192.
- Taylor, K.E., Stouffer, R.J., Meehl, G.A., 2012. An overview of CMIP5 and the experiment design. *Bull. Amer. Meteorol. Soc.* 93, 485–498.
- Tjallingii, R., Claussen, M., Stuut, J.B.W., Fohlmeister, J., Jahn, A., Bickert, T., Lamy, F., Rohl, U., 2008. Coherent high- and low-latitude control of the northwest African hydrological balance. *Nat. Geosci.* 1, 670–675.
- Trenberth, K.E., Stepaniak, D.P., Caron, J.M., 2000. The global monsoon as seen through the divergent atmospheric circulation. *J. Clim.* 13, 3969–3993.
- Wang, B., Ding, Q., 2008. Global monsoon: dominant mode of annual variation in the tropics. *Dyn. Atmos. Oceans* 44, 165–183.
- Wang, B., Liu, J., Kim, H.J., Webster, P.J., Yim, S.Y., 2012. Recent change of the global monsoon precipitation (1979–2008). *Clim. Dyn.* 39, 1123–1135.
- Wang, P.X., 2009. Global monsoon in a geological perspective. *Chin. Sci. Bull.* 54, 1113–1136.
- Wang, X., Auler, A.S., Edwards, R.L., Cheng, H., Cristalli, P.S., Smart, P.L., Richards, D.A., Shen, C.C., 2004. Wet periods in northeastern Brazil over the past 210 kyr linked to distant climate anomalies. *Nature* 432, 740–743.
- Wang, Y., Cheng, H., Edwards, R.L., Kong, X., Shao, X., Chen, S., Wu, J., Jiang, X., Wang, X., An, Z., 2008. Millennial- and orbital-scale changes in the East Asian monsoon over the past 224,000 years. *Nature* 451, 1090–1093.
- Weber, S.L., Drury, A.J., Toonen, W.H.J., van Weele, M., 2010. Wetland methane emissions during the last glacial maximum estimated from PMIP2 simulations: climate, vegetation, and geographic controls. *J. Geophys. Res.* 115 <http://dx.doi.org/10.1029/2009JD012110>. D06111.
- Webster, P.J., Magaña, V.O., Palmer, T.N., Shukla, J., Tomas, R.A., Yanai, M., Yasunari, T., 1998. Monsoons: processes, predictability, and the prospects for prediction. *J. Geophys. Res.* 103 (C7), 14451–14510.
- Weldeab, S., Lea, D.W., Schneider, R.R., Andersen, N., 2007. 155,000 years of west African monsoon and ocean thermal evolution. *Science* 316, 1303–1307.
- Wu, H., Guiot, J., Brewer, S., Guo, Z., 2007. Climatic changes in Eurasia and Africa at the last glacial maximum and mid-Holocene: reconstruction from pollen data using inverse vegetation modelling. *Clim. Dyn.* 29, 211–229.
- Yan, Z., Petit-Maire, N., 1994. The last 140 ka in the Afro-Asian arid/semi-arid transitional zone. *Paleogeogr. Paleoclimatol. Paleoecol.* 110, 217–233.
- Yanase, W., Abe-Ouchi, A., 2007. The LGM surface climate and atmospheric circulation over East Asia and the North Pacific in the PMIP2 coupled model simulations. *Clim. Past* 3, 439–451.
- Yang, X., Scuderi, L.A., 2010. Hydrological and climatic changes in deserts of China since the late Pleistocene. *Quat. Res.* 73, 1–9.
- Yu, G., Chen, X., Ni, J., Cheddadi, R., Guiot, J., Han, H., Harrison, S.P., Huang, C., Ke, M., Kong, Z., Li, S., Li, W., Liew, P., Liu, G., Liu, J., Liu, Q., Liu, K.B., Prentice, I.C., Qui, W., Ren, G., Song, C., Sugita, S., Sun, X., Tang, L., Van Campo, E., Xia, Y., Xu, Q., Yan, S., Yang, X., Zhao, J., Zheng, Z., 2000. Palaeovegetation of China: a pollen data-based synthesis for the mid-holocene and last glacial maximum. *J. Biogeogr.* 27, 635–664.
- Zhou, B.T., Zhao, P., 2009. Inverse correlation between ancient winter and summer monsoons in East Asia? *Chin. Sci. Bull.* 54, 3760–3767.
- Ziegler, M., Tuenter, E., Lourens, L.J., 2010. The precession phase of the boreal summer monsoon as viewed from the eastern mediterranean (ODP site 968). *Quat. Sci. Rev.* 29, 1481–1490.